Research article

Yulin Wang, Zhanghua Han, Yong Du and Jianyuan Qin*

Ultrasensitive terahertz sensing with high-Q toroidal dipole resonance governed by bound states in the continuum in all-dielectric metasurface

Abstract: Toroidal dipole (TD) with weak coupling to the electromagnetic fields offers tremendous potential for advanced design of photonic devices. However, the excitation of high quality (Q) factor TD resonances in these devices is challenging. Here, we investigate ultrahigh-Q factor TD resonances at terahertz frequencies arising from a distortion of symmetry-protected bound states in the continuum (BIC) in all-dielectric metasurface consisting of an array of high-index tetramer clusters. By elaborately arranging the cylinders forming an asymmetric cluster, two distinct TD resonances governed by BIC are excited and identified. One is distinguished as intracluster TD mode that occurs in the interior of tetramer cluster, and the other one is intercluster TD mode that arises from the two neighboring clusters. Such TD resonances can be turned into ultrahigh-Q leaky resonances by controlling the asymmetry of cluster. The low-loss TD resonances with extremely narrow linewidth are very sensitive to the change in the refractive index of the surrounding media, achieving ultrahigh sensitivity level of 489 GHz/RIU. These findings will open up an avenue to develop ultrasensitive photonic sensor in the terahertz regime.

Keywords: all-dielectric metasurface; bound states in the continuum; terahertz sensing; toroidal dipole.

*Corresponding author: Jianyuan Qin, Center for Terahertz Research, China Jiliang University, Hangzhou 310018, China,
E-mail: jyqin@cjlu.edu.cn. https://orcid.org/0000-0002-8774-0591
Yulin Wang and Yong Du, Center for Terahertz Research, China Jiliang University, Hangzhou 310018, China
Zhanghua Han, School of Physics and Electronics, Shandong Normal University, Jinan 250358, China. https://orcid.org/0000-0002-4177-2555

1 Introduction

Terahertz (THz) technology has made great achievements in a large number of applications including biomedical diagnosis [1], security screening [2], and wireless communication [3] in recent years. The most important and promising applications of THz technology are in nondestructive imaging and label-free sensing due to the its peculiar properties of strong penetrability in nonconducted materials, low photon energy, and spectral fingerprints for biomolecules [4–6]. In THz region, most molecules exhibit strong absorption and dispersion due to their rotational and vibrational transitions. These transitions are rendered as spectral fingerprints that are specific to the molecule, thus achieving the molecular detection and reorganization [4, 7]. However, the limited sensitivity of THz technology has already restricted and hindered its further application in sensing. According to this problem, several routes have been proposed as THz signal amplification approaches to attain competitive sensitivity for sensing applications [8–10]. Among them, THz sensors based on all-dielectric metamaterial structures show a remarkable sensitivity due to their lower intrinsic losses and higher quality (Q) factors. All-dielectric metamaterial, artificial completely nonmetallic materials consisting of periodically arranged subwavelength elements, exhibit unique electromagnetic properties [11]. As a promising alternative to metallic metamaterial, all-dielectric metamaterial can support Mie resonances with small dissipation and low thermal conductivity [12, 13], providing a good platform for highly efficient THz devices [14–16]. The strong confinement of electromagnetic field in the all-dielectric metamaterial enhances the light–matter interaction and enables the sensitive detection of analytes. Therefore, all-dielectric metamaterial has received special attention and been widely studied for ultrasensitive sensing recently. Mie resonances such as electric dipole (ED) and magnetic dipole (MD) can be easily excited in all-dielectric metamaterial structures [13]. However, the excitation of toroidal

dipole (TD) in these systems is still challenging. The TD can be viewed as a circular head-to-tail arrangement of magnetic or electric dipoles that are squeezed into a single point [17]. It is the virtually unknown third family of electromagnetic multipole, the toroidal multipole, which along with the familiar magnetic and electric multipole is necessary for the complete multipole representation of an arbitrary radiating source [18, 19]. The essence of TD can be divided into magnetic TD and electric TD according to the polarization currents distribution. The magnetic TD is created by polarization currents flowing on a surface of a torus along its meridians, and is represented head-to-tail magnetic moments, while the electric TD is produced by the ring of the polarization current flowing along the toroidal direction, and is represented as a ring of the electric dipole moments configuration [20]. Owning to its relatively weak coupling to the incident electromagnetic wave, TD is naturally masked by much stronger electromagnetic effects, so its excitation is very difficult to be detected. However, the use of metamaterial concept makes the observation and detection of TD response possible [21–24]. This concept enables us to access to exotic and novel optical phenomena of TD by artificially structuring media on a subwavelength scale [25, 26]. The TD response in metamaterial was theoretically proposed [27], and then experimentally demonstrated at the microwave regime by using the metallic metamaterial composed of three-dimensional (3D) resonators [21]. It was recently discovered that even two-dimensional (2D) metallic or all-dielectric metamaterial (i.e., metasurface) structures could support strong TD resonances in the microwave [28, 29], THz [30, 31], infrared [32, 33], and visible [34, 35] regions. Compared to the 3D metamaterial structures, the fabrication of 2D metasurface structure is simpler and easier, which promotes the research and utilization of TD response. The TD resonances in all-dielectric metasuface are high-Q in nature, and could provide sufficiently large field confinement necessary for a variety of applications due to the low material loss of all-dielectric materials. Strong TD excitations were observed in all-dielectric metasurface consisting of clusters of subwavelength high-index dielectric cylinders. Its electric field was concentrated in the dielectric-free regions of the unit cell in a spot smaller than $\lambda/5$, which makes the metasurface a viable platform for sensing or enhancement of light absorption [30]. A high-index microtube-based all-dielectric metasurface structure was proposed, and a low-loss TD resonance could be obtained with a high-Q factor of 118 as well as a strong local field enhancement in the deep subwavelength scale, offering application potentials such as sensing, energy harvesting, and nonlinear optical effects

[36]. It was demonstrated that all-dielectric metasurface composed of properly arranged cluster could excite strong TD resonance with high-Q feature, each cluster consisted of two pairs of dielectric nanodisks with different radii. Such TD response originated from a trapped mode that appeared due to the symmetry breaking in the cluster. The unique field configuration of TD mode enabled this metasurface to serve as a tool for efficient light–matter interaction for enhanced absorption, nonlinear response, and sensing [32]. By arranging two pairs of high-index disks with different heights in a cluster, the out-of-plane symmetry breaking was introduced to the metasurface structure. In this case, a strong TD resonance with an ultrahigh-Q factor of 3189 could be excited. The electric field was intensively confined in the gap between the disks for the TD mode, indicating the strong interaction between the THz waves and analytes. The simulated refractive index sensing sensitivity of 438 GHz per refractive index unit (RIU) could be obtained [37]. The TD resonances in all-dielectric metasurface structures have gained widespread attention and have inspired a new wave of research in the field of optical device design. However, the current research on this topic is mainly focus on the intriguing phenomena in the presence of TD excitations, while little has been done on the sensing applications using TD resonances.

For sensing applications, high-Q factor resonance that has extremely narrow linewidth is typically desired, which shows ability in detection of a small frequency shift that arises due to the trace analyte or the weak environmental variation. Moreover, the intensity of the resonance should be strong enough to be easily detected in a noisy environment [38]. One particularly effective approach to achieve extremely high-Q resonance is based on the bound state in the continuum (BIC). The BIC that originally appears in quantum mechanics represents a general wave phenomenon observed in acoustics, hydrodynamics, and optics. Later, it was explained in terms of destructive interference when the coupling constants with all radiating waves vanish accidentally by continuous tuning of parameters. If the coupling constants vanish due to the symmetry, such BIC is symmetry-protected [39]. A true BIC exist only in ideal lossless infinite structures or extreme values of parameters, and shows an infinite-Q factor and vanishing resonance linewidth [40, 41]. In practice, BIC can be realized as quasi-BIC by creating a leaky resonance through symmetry breaking, where both Q factor and the resonance linewidth become finite. The concept of manipulating the transition between the symmetry-protected BIC and leaky resonance was first proposed for metallic metamaterial composed of split-ring resonators [42], and then it was developed for all-dielectric

metasurface [43–46]. It was revealed that all-dielectric metasurface with symmetry breaking of unit cell can support high-Q factor Fano resonances [41, 43] or TD resonances [44, 45] arising from the distortion of symmetry-protected BIC. Such a BIC-inspired mechanism makes it possible to access extremely high-Q resonances and giant enhancement of electromagnetic fields [47], realizing many useful functionalities including lasing [48], polarization [49], and sensing [50]. Fano resonances are famous for supporting enhanced sensitivities, but they fail in detecting molecules at extremely low-level concentrations. It was reported that TD resonances could bridge this gap in the field of sensing and showed the exotic ability to detect extremely low-weight biomarkers at ultralow densities [22, 51]. However, limited attention has been paid to sensing utilizing TD resonances at THz frequencies governed by BIC that will provide a more efficient platform for ultrasensitive sensors.

In this paper, we demonstrate ultrasensitive sensing based on TD resonances driven by BIC at THz frequencies in an all-dielectric metasurface structure with a periodic array of asymmetric tetramer clusters. The excitation of two TD modes is achieved through introducing symmetry breaking and forming spatial asymmetric tetramers. It is confirmed from the displacement current and field patterns that the two TD resonances are derived from intracluster TD and intercluster TD, respectively. By controlling the asymmetric parameter a, the TD resonances can transform from symmetry-protected BIC into quasi-BIC with ultrahigh-Q factor of 1.2×10^5 at $a = 0.4$ μm, revealing that these resonances are driven by BIC. The detection of analyte thickness indicates that the all-dielectric metasurface function better in sensing thin analyte, and it is applicable to the detection of trace analyte. The refractive index sensing shows that the sensitivity of our structure can reach up to 489 GHz/RIU that corresponds a corresponding figure of merit (FoM) of 25,352, and this sensitivity is higher than that of the previous reported all-dielectric metasurface THz sensors [8, 37]. Our findings present an effective approach for realizing ultrasensitive sensing at THz frequencies.

2 Structure design

Figure 1A illustrates the schematic of the THz asymmetric all-dielectric metasurface structure. It consists of a periodic array of tetramer clusters arranged in a square lattice. Each cluster (unite cell) contains four high-index cylinders deposited on a quartz substrate (refractive index being $n = 2$). The geometric parameters of the unit cell are presented in Figure 1B. Here, the lattice constant is $P_x = P_y = P = 63$ μm, the cylinder radius is $r = 11$ μm, the cylinder height $h = 11$ μm. Figure 1C shows the top view of the unit cell in the x–y plane to more clearly illustrate the asymmetry of the structure. The asymmetric parameter a represents the distance that the two cylinders move in the opposite direction along y-axis. Specifically, $a = 0$ means there is no movement for the two cylinders, and the unit cell is symmetric in the x–y plane. In this case, the centers of four cylinders are arranged in a square with a length of $L = 26$ μm (shown as white dashed lines). For $a \neq 0$, it means the introduction of symmetry breaking in which two cylinders of the tetramer move a distance of a in the opposite direction along y-axis, while the positions of the other two cylinders are fixed in their original positions. We define $a > 0$ to represents the two cylinders both move away from the x-axis, while $a < 0$ refers to the two cylinders both move close to x-axis. Lithium tantalate (LiTaO$_3$) is chosen as building material for the tetramer clusters due to its negligible dissipation loss at THz frequencies [30]. The complex dielectric permittivity of LiTaO$_3$ can be expressed as the Lorenz-type dispersion $\varepsilon = \varepsilon_\infty (\omega^2 - \omega_L^2 + i\omega\gamma)/(\omega^2 - \omega_T^2 + i\omega\gamma)$. Here, the frequency of transverse optical photons is $\omega_T/2\pi = 26.7$ THz, the frequency of longitudinal optical photons is $\omega_L/2\pi = 46.9$ THz, the damping factor is $\gamma/2 = 0.94$ THz, and $\varepsilon_\infty = 13.4$ is the limiting value for frequencies much higher than ω_L, the permittivity of LiTaO$_3$ can be set as 41.4 when the frequencies are lower than ω_L. Numerical simulations on the electromagnetic properties as well as the spectral responses of all-dielectric metasurface were performed using finite element method (FEM) with the commercially available Comsol Multiphysics (Version 5.3) [52], where the Floquet-periodic boundary conditions were imposed on four sides of the unit cell, and the excitation field was a y-polarized plane wave propagating along the z-axis.

For an all-dielectric metasurface structure consisting of an array of equidistantly spaced subwavelength dielectric cylinders, each cylinder behaves as an individual resonator supporting a set of electric and magnetic multipole modes [30]. Electromagnetic coupling of these modes to the field of the incident wave can become a resonant response for the whole metasurface, which is depending on the geometric parameters of the cylinders, their dielectric constant, and the polarization of the incident wave. The ED and MD resonances are two basic modes that can be readily excited in the metasurface structure. However, the excitation of TD response is challenging, and it needs to engineer a structure that is able to support a loop of magnetic or electric moments configuration [32]. In our present study, such structure is formed by periodically arranging tetramer
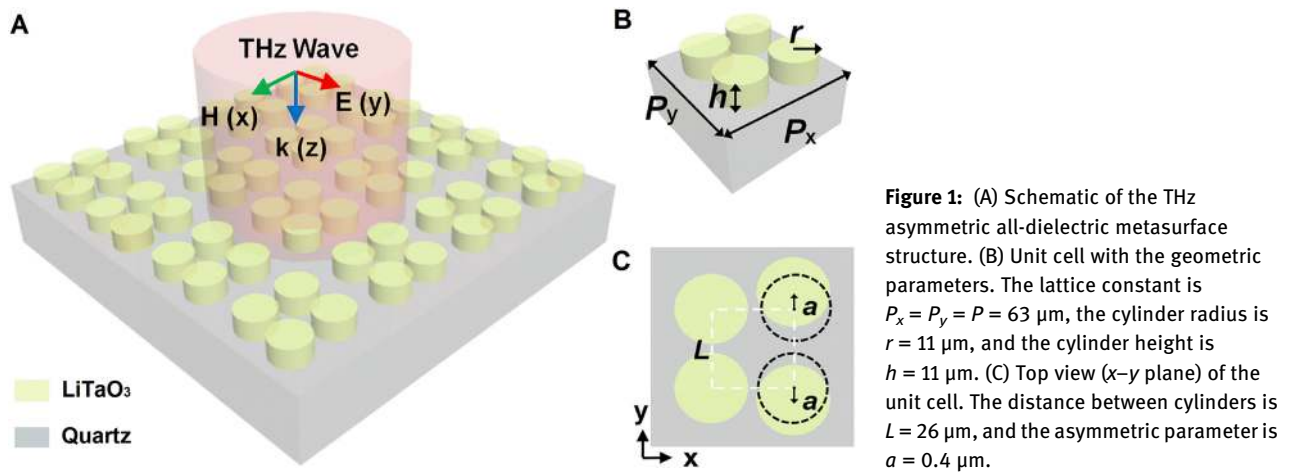
Figure 1: (A) Schematic of the THz asymmetric all-dielectric metasurface structure. (B) Unit cell with the geometric parameters. The lattice constant is $P_x = P_y = P = 63$ μm, the cylinder radius is $r = 11$ μm, and the cylinder height is $h = 11$ μm. (C) Top view (x–y plane) of the unit cell. The distance between cylinders is $L = 26$ μm, and the asymmetric parameter is $a = 0.4$ μm.

clusters and each cluster itself appears as a resonator where four dielectric cylinders are assembled closer to each other. In this case, the overall metasurface response is mainly determined by the electromagnetic coupling between the resonators inside the cluster rather than by the individual cylinders. Besides, the mutual influence of neighboring clusters also has an effect on the electromagnetic response [28, 45]. As a result, it will turn out to be a complex collective behavior of modes being very different from that of the ED and MD modes of individual cylinders.

3 Results and discussions

As the first step, we demonstrate the existence of TD resonances in our asymmetric all-dielectric metasurface structure for y-polarization. In this case, the THz wave is vertically incident on the metasurface along the z-direction with an electric field polarized along the y-axis. For the symmetric structure ($a = 0$ μm), only one resonance can be observed at 2.08 THz in the transmission spectrum. It is evident from displacement current and field patterns that this resonance corresponds to the MD mode and thus is marked as MD [32], as shown in the first column in Figure 2D. This MD resonance is distinguished as a collective response of four longitudinal MDs, the displacement currents at the resonance exhibit a circular behavior twisting around the center of each cylinder in the x–y plane and induce four magnetic moments inside the cylinders that oscillate in antiphase along z-axis. The electric field at the MD resonance is confined at the center part of the cluster, which indicates the MD mode existing inside this area. As symmetric breaking is introduced to this metasurface structure ($a = 0.4$ μm), as shown in Figure 2B, besides the MD resonance previously discussed, two additional ultrasharp resonances located at 2.25 and 2.41 THz

that originate from TD modes appear in transmission spectrum, which are marked as TD_1 and TD_2, respectively. The larger versions of transmission spectra for these two resonances are also plotted in the insets of Figure 2B for a clearer view. The displacement current and field enhancement patterns of these two resonances were also calculated, and are plotted in the second and third columns in Figure 2D to gain insight into their nature. For TD_1, the displacement currents thread all four cylinders of a tetramer cluster and are distributed in a closed loop, the magnetic field is located inside the cylinders and at the center part of the tetramer with circular patterns inside each cylinder, see the inset of second column in Figure 2D. In this case, a particular vortex of electric field within the cluster can be generated, and producing the electric TD mode. Figure 2C (left) illustrates the conceptual description of TD_1, the green circles with arrows show the magnetic field, the red circles with arrows represent the displacement currents, and the blue arrows are the excited TD moments (**T**). Obviously, the magnetic field flows on a surface of a torus along its meridians, such a flow can induce a distinct electric vortex with head-to-tail configuration encircling the center of the cluster along the toroidal direction, which excites TD mode within the cluster. Therefore, we distinguish TD_1 as intracluster TD resonance because it is produced in the interior of tetramer cluster. As for TD_2, the displacement currents do not have a closed loop arrangement within the cluster, but it rather appears a mode distributed between two neighboring clusters. The displacement currents penetrate four cylinders of two neighboring clusters, forming a particular vortex of electric field between them. In this case, the magnetic field distributes outside the area formed by the two neighboring clusters with circular patterns inside each cylinder, see the inset of third column in Figure 2D. The conceptual description of TD_2 is shown in Figure 2C (right), it can be see that the magnetic field circulates on a surface of a torus along its meridians

between these two neighboring clusters (green circles with arrows), such a circle induces a distinct head-to-tail pattern of electric field wreathes the center of the area formed by the two neighboring clusters along the toroidal direction, which excites TD mode between two neighboring clusters. Therefore, TD_2 stems from the intercluster coupling of cylinders from two neighboring clusters and can be recognized as intercluster TD resonance. These results show that these two TD modes possess far stronger electric filed enhancement compared with the MD mode. More importantly, the electric filed for TD modes are concentrated at the gaps between the cylinders (i.e., the air area). In this case, more analytes will be covered by the electric field at the TD modes, achieving a better spatial overlap and stronger light–matter interactions than the MD mode.

To quantitatively estimate the dominant TD resonance in TD_1 and TD_2 of our proposed structure, we perform a multipole decomposition under the Cartesian coordinate [53, 54]. Five terms, namely, electric dipole **P**, magnetic dipole **M**, electric quadrupole **Qe**, magnetic quadrupole **Qm**, and electric toroidal dipole **T** were taken into account (higher orders of the multipole expansion were neglected in the computations due to their very small contribution), and the decomposition results for the unit cell (Type 1, the red dashed box in Figure 3A) are shown in Figure 3B. It can be

seen from the inset of Figure 3B that TD_1 (2.25 THz) can be observed, and it is dominated by the electric toroidal dipole **T** although the contribution from the magnetic quadrupole **Qm** is fairly great. However, the electric dipole **P**, magnetic dipole **M**, and electric quadrupole **Qe** are dramatically suppressed in this case. For TD_2 (2.41 THz), since this resonance is a result of the intercluster coupling, it does not appear in the multipole decomposition performed for the unit cell (Type 1). Therefore, it needs to be identified from the electromagnetic distribution (Figure 2D). To demonstrate each multipole and their contributions to the TD_2, the multipole decomposition for the other unit cell (Type 2, the blue dashed box in Figure 3A) was also performed, and the results are shown in Figure 3C. In this case, TD_2 can appear and for this resonance, electric toroidal dipole **T** is dominant, with a secondary contribution of the magnetic quadrupole **Qm**. Similarly to the TD_1, the electric dipole **P**, magnetic dipole **M**, and electric quadrupole **Qe** are strongly suppressed. Under the condition of the metasurface consisting of this unit cell (Type 2), TD_1 is from the intercluster coupling, thus it cannot be observed in the multipole decomposition performed for Type 2. These results again demonstrate that TD_1 and TD_2 are both electric TD resonances, the former is derived from intercluster while the latter is from the intracluster.
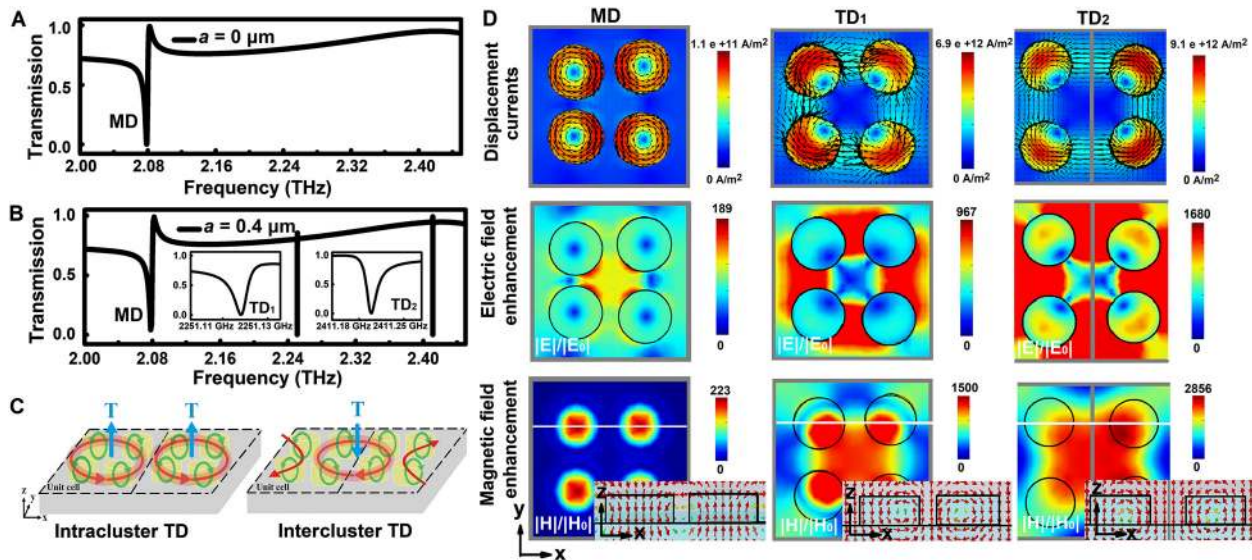

Figure 2: Transmission spectra of the metasurface with an asymmetric parameter (A) $a = 0$ μm and (B) $a = 0.4$ μm, the insets are larger versions of transmission spectra for TD_1 and TD_2, respectively. (C) The conceptual descriptions of intracluster TD and intercluster TD, the dashed box indicates the unit cell of the metasurface, the green circles with arrows show the magnetic field, the red circles with arrows represent the displacement currents, and the blue arrows are the excited TD moments. (D) Cross-sectional patterns of displacement currents (arrows represent the directions of displacement currents), electric field enhancement, and magnetic field enhancement at the three resonances in the $x–y$ plane with z-axis corresponding to the half-height of the cylinder. The insets in (D) show the cross-sectional patterns of magnetic field in $x–y$ plane with y-axis corresponding to the position of white line in the distribution of the magnetic field enhancement in the $x–y$ plane, the red arrows show the directions of magnetic field. The gray line refers to the boundary of the two neighboring clusters.
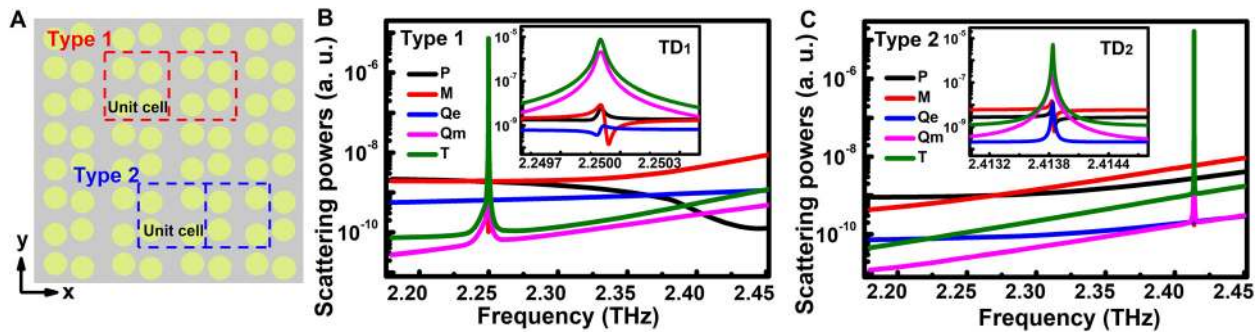
Figure 3: (A) Top view (*x–y* plane) of the asymmetric metasurface structure, the red dashed boxes indicate the unit cell of Type 1, and the blue dashed boxes indicate the unit cell of Type 2. The scattering powers of multipole decomposition for (B) the unit cell of Type 1 and (C) the unit cell of Type 2, where **P, M, Qe, Qm,** and **T** are the ED, MD, electric quadrupole, magnetic quadrupole, and electric toroidal dipole, respectively. The insets are larger versions of the scattering powers for TD_1 and TD_2.

To demonstrate that the two TD resonances for the asymmetric metasurface structure ($a = 0.4\,\mu m$) appear only in the condition of *y*-polarization, the incident electric field polarized along the *x*-axis is also investigated, and the comparative results of transmission spectra for *x*- and *y*-polarization are shown in Figure 4A. It is confirmed that the two TD resonances exist under *y*-polarization condition (black solid line), and will disappear for *x*-polarization (red dashed line). Under the condition of *x*-polarization, only one resonance can be excited, which is at exactly the same position as MD resonance is in the case of *y*-polarization. The analysis for the displacement current and field enhancement patterns of this resonance show that it is derived from the MD mode and can be recognized as the collective response of four longitudinal MDs. As can be seen in Figure 4B, like that of MD resonance in the case of *y*-polarization, the electric field at this resonance is mainly located in the center part of the tetramer. The displacement currents show a circular behavior encircling around the center of each cylinder. This ring-like displacement currents' pattern produces four magnetic moments oriented along the *z*-axis. Also note that the displacement currents inside the lower left and upper right cylinders encircle in the opposite direction to those of their corresponding cylinders for *y*-polarization, see the inset in Figure 4B. Thus, the magnetic moments inside these two cylinders oscillate in the opposite direction compared to the case of *y*-polarization. These results demonstrate that the MD resonance is polarization-insensitive, and it appears in the transmission spectra for both *y*-polarized and *x*-polarized electric fields. It is also confirmed that the excitation of TD modes under *y*-polarization is mainly because of the symmetry breaking.

To further study these two TD resonances, we calculated the transmission spectra of this metasurface structure with different asymmetric parameter *a* ranging from −1.6 to

1.6 μm, and the results are shown in Figure 5A. Clearly, MD resonance can be spotted for all *a* values, and its frequency position as well as linewidth remains almost constant. However, the two TD resonances both slightly shift toward lower frequency with *a* close to 0 μm, and their linewidths are both becoming narrower. When *a* equals to 0 μm, these two TD resonances vanish, which means no leaky energy from the bound state to the free space and demonstrates the existence of two symmetry-protected BICs [39]. As *a* continues to increase or decrease, these two resonances appear again with a visible linewidth. This is due to the fact that the movements of two cylinders within a cluster perturb the in-plane symmetry of the metasurface structure and transform the above symmetry-protected BICs to quasi-BICs. As a result, two obvious TD resonances that originate from the interference between discrete states supported by the tetramer array and the continuum free-space radiation can be produced [44]. For *a* > 0 μm, the two TD resonances both have a slight red shift, and their linewidths become wider as *a* increases. However, these two TD resonances appear to be robust for *a* < 0 μm, showing a weak reshaping of the resonance when *a* decreases. This phenomenon is due to the difference in electric field enhancement distribution between *a* > 0 μm and *a* < 0 μm, as shown in Figure 5B and C. It can be seen that for *a* = 1.6 μm, the electric fields of TD_1 and TD_2 are mainly concentrated between the two nonperturbed cylinders. When *a* = −1.6 μm, their electric fields are largely localized between the two perturbed cylinders (indicated as the white solid circles), thus their resonance characteristics are more sensitive to the perturbation in these two cylinders.

The symmetric metasurface structure ($a = 0\,\mu m$) supports two symmetry-protected BICs with disappeared resonance linewidths and infinite-*Q* factors. For asymmetric metasurface structure, the corresponding-*Q* factors
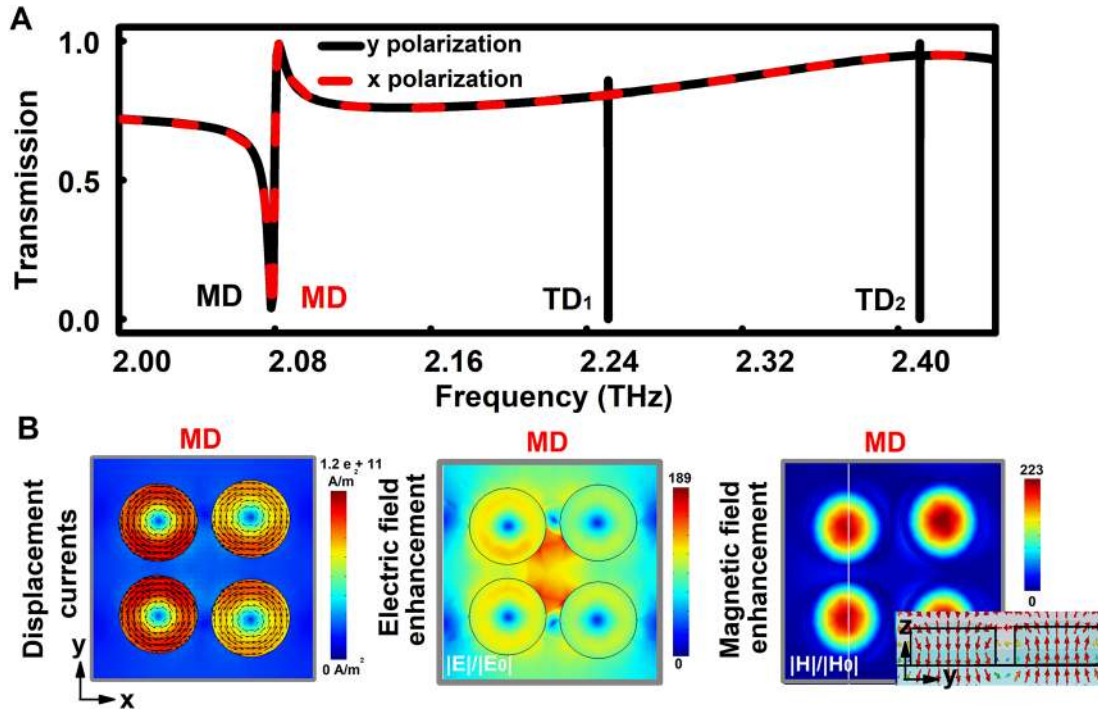
Figure 4: (A) Transmission spectra of the asymmetric metasurface structure (*a* = 0.4 μm) under the *y*-polarization (black solid line) and *x*-polarization (red dashed line). (B) Cross-sectional patterns of displacement currents, electric field enhancement, and magnetic field enhancement at MD resonance for *x*-polarization in the *x*–*y* plane with *z*-axis corresponding to the half-height of the cylinder.
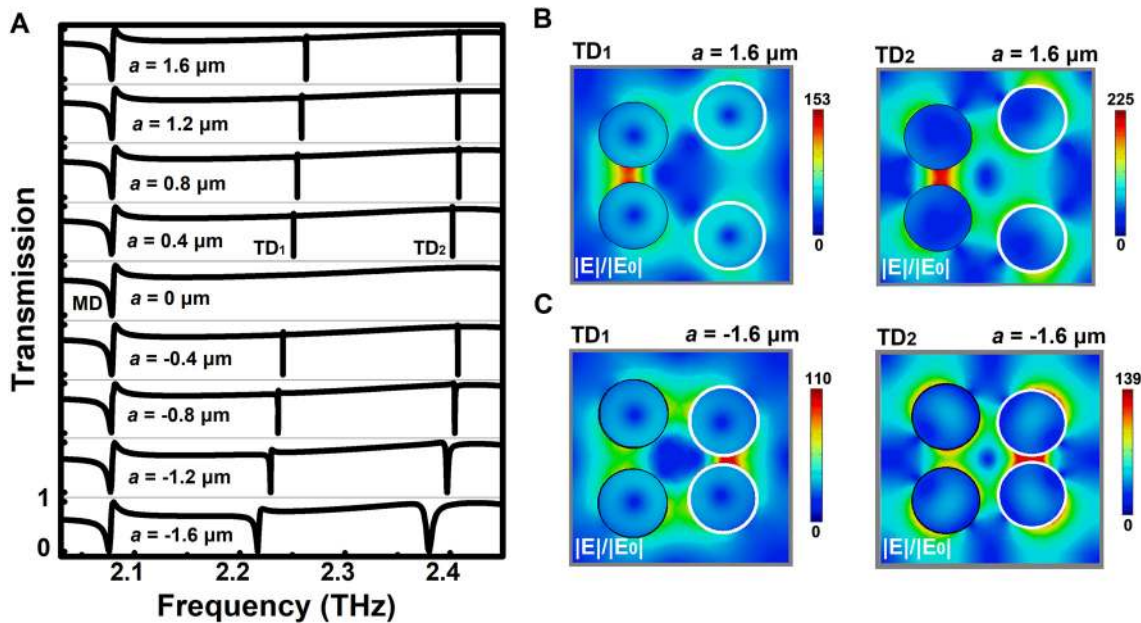

Figure 5: (A) Transmission spectra of all-dielectric metasurface with different asymmetric parameter *a*. The cross-sectional patterns of electric field enhancements for TD_1 and TD_2 at (B) *a* = 1.6 μm and (C) *a* = −1.6 μm in the *x*–*y* plane with *z*-axis corresponding to the half-height of the cylinder, the white solid circles represent the perturbed cylinders.

of TD_1 and TD_2 at different asymmetric parameter *a* are calculated, the *Q* factor here is defined as $f_0/\Delta f$, where f_0 is the frequency of the resonance, and Δf is the full width at half-maximum (FWHM) of the resonance. Figure 6A and B shows the log-log plot of the-*Q* factor versus the absolute value of asymmetric parameter *a* (|*a*|) for TD_1 and TD_2,
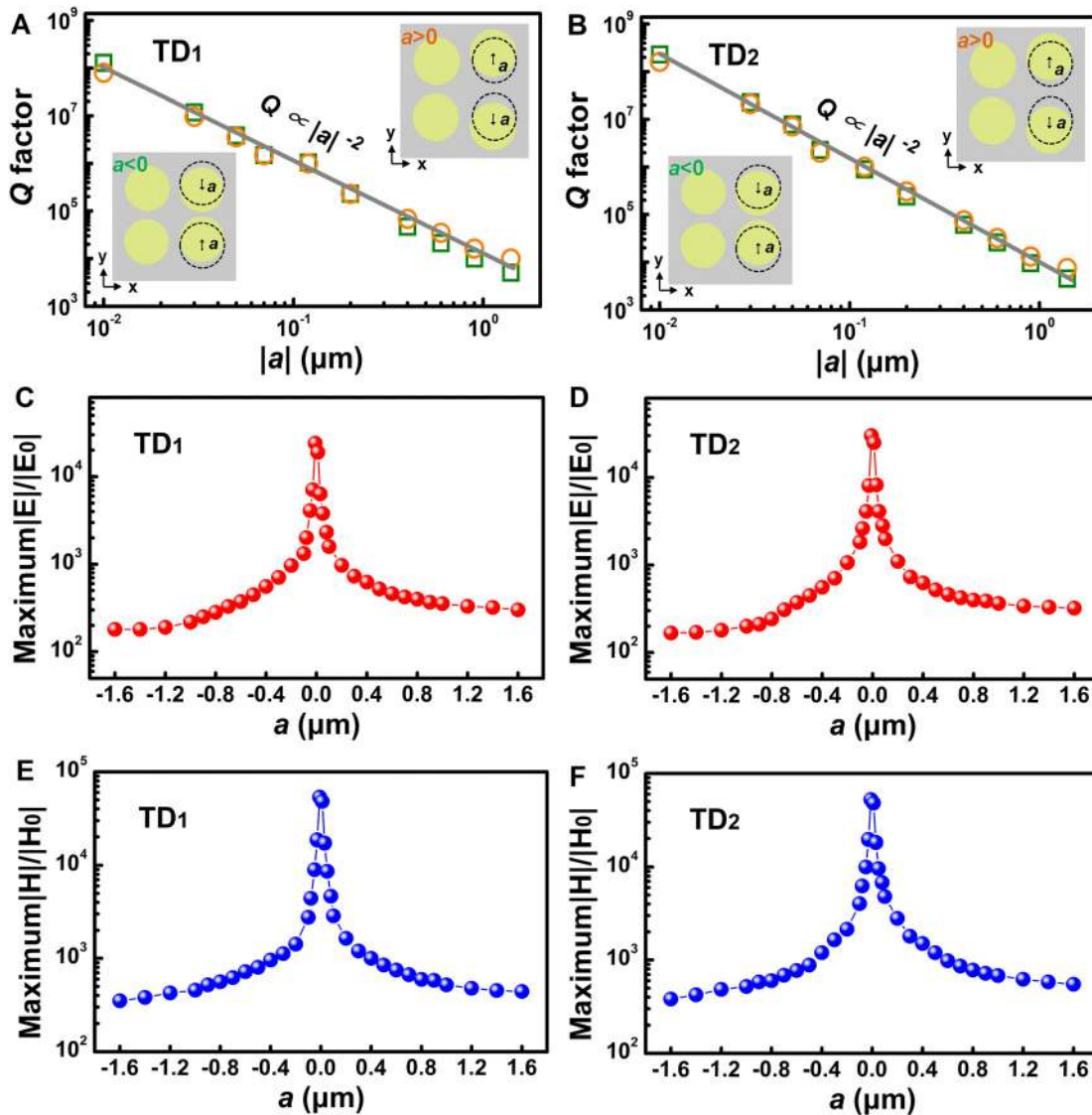
Figure 6: The log-log plot of Q factors as a function of the absolute value of asymmetric parameter $|a|$ for (A) TD_1 and (B) TD_2, the orange hollow circles represent the case of $a > 0$ μm, and the green hollow squares are the case of $a < 0$ μm. The gray lines show the inverse quadratic dependence of $|a|$. The field enhancement in a logarithm scale of electric field for (C) TD_1 and (D) TD_2 and magnetic field for (E) TD_1 and (F) TD_2 at a location of z-axis corresponding to the half-height of the cylinders with respect to the asymmetric parameter a.

respectively, the orange circles represent the case of $a > 0$ μm, and the green squares are the case of $a < 0$ μm. It can be seen that for two structures with an equivalent $|a|$ value, their TD resonances have nearly the same Q factors although these two cases form different metasurface structures with resonance frequencies lying at different positions. The evolution of Q factor on the asymmetric parameter $|a|$ follows the inverse quadratic law $Q = Q_0 |a|^{-2}$, where Q_0 is a constant determined by the metasurface being independent of $|a|$ [39, 41]. The Q factor for TD_1 increases to an ultrahigh value of 1.28×10^8 as $|a|$ approaches to 0 μm, and is becoming infinite at $a = 0$ μm. The Q factor of

TD_2 has a similar variation trend as that of TD_1 and reaches an ultrahigh value of 2.3×10^8 near $|a| = 0$ μm, and achieves an infinite Q factor at $a = 0$ μm. These results confirm that the two TD resonances are both BIC-inspired and thus are governed by BIC. The cluster with symmetry breaking is necessary to obtain a sharp TD quasi-BIC resonance where its frequency position and linewidth can be controlled by the asymmetric parameter. The excitations of such TD quasi-BIC resonances with ultrahigh-Q factor are associated with the strong near field enhancement. Figure 6C–F shows the electric field and magnetic field enhancements of TD_1 and TD_2 in a log scale at a location of z-axis

corresponding to the half-height of the cylinders at different asymmetric parameter a, respectively. When $|a|$ decreases from 1.6 to 0.4 µm, all fields enhance gradually. Continuing to decrease $|a|$, field enhancements greatly increase to reach an extremely high value. At $|a|$ = 0.01 µm, the electric field enhancements are 24,200 and 30,024 for TD_1 and TD_2, and the corresponding magnetic field enhancements can be as high as 48,200 and 53,400, respectively. It can be found that the field enhancements of TD_2 are larger than that of TD_1. Such strong fields are mainly distributed in the gaps among the cylinders where they can effectively interact with analytes, which will have huge advantages in sensing application.

To study the dependence of transmission spectra on different geometric parameters, we calculate the transmission spectra of the asymmetric metasurface structure with different geometric parameters when the asymmetric parameter a is set to 0.4 µm, other geometric parameters are the same as the parameters used in Figure 2 except the variable parameter shown in each figure. All the geometric parameters change with a step of 1 µm, and the results are

shown in Figure 7. It can be seen that all resonances, including MD, TD_1, and TD_2 experience a red shift while their linewidths are little changed as h increases from 7 to 11 µm, see Figure 7A, and the shift for TD_2 is the most nonobvious among the three resonances. The increase of r from 7 to 11 µm also results in a red shift of all resonances, as shown in Figure 7B, and the shifts for all three resonances are more pronounced than those of increasing h. Slight red shifts for TD_1 and TD_2 can be observed with P increasing from 61 to 65 µm due to the increase of effective refractive index of the structure, see Figure 7C. However, the position of MD keeps almost unchanged in this case. On the contrary, all resonances show a slight blue shift when L increases from 24 to 28 µm, and their intensities become weaker due to a weaker coupling effect between the cylinders with L increasing, see Figure 7D. It is worth noting that the shifts for MD and TD_2 are so slight as to be almost unchanged. Comparing the impacts of different geometric parameters on the transmission spectra of the asymmetric metasurface structure, it can be seen that the position of these three resonances is more sensitive to r and h, while
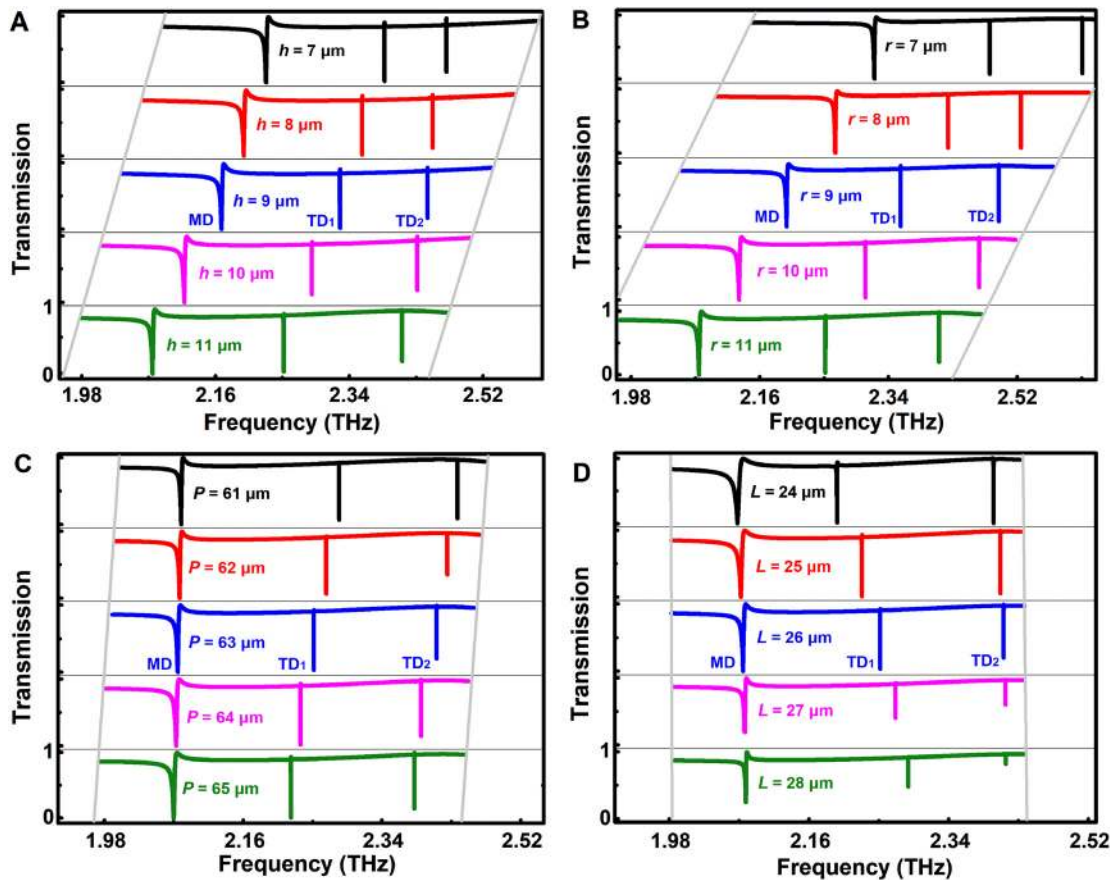

Figure 7: Transmission spectra of the asymmetric metasurface structure (a = 0.4 µm) with different (A) height h, (B) radius r, (C) period P, and (D) distance L.

their resonance intensities are mainly affected by L. However, all the three resonances appear to be robust for P than other geometric parameters. More specifically, the r and h of cylinder have a far greater influence on MD resonance than the parameters L and P. This is due to the fact that MD mode, as a basic set of magnetic multipole mode, its resonance characteristic mainly depends on the geometric parameters of cylinder. For TD mode, as a complex collective response, the influence of parameter r on it is greater than those of other geometric parameters. Based on these results, the TD resonances of the asymmetric metasurface structure can be easily tailored by adjusting different geometric parameters.

The significance of sensing using THz spectroscopy lies in the fact that biomolecules such as DNA have vibrational resonances located in the THz domain [4, 6]. The refractive index of biomolecule usually varies from 1.4 to 2.0, which can induce the detectable resonance shift of the metasurface structure. According to the analysis of field enhancement, the frequency shift of TD_2 resonance is selected as an indicator to evaluate the sensing performance of this asymmetric metasurface structure ($a = 0.4\,\mu m$). Here, the analyte with a refractive index of 1.6 is deposited on the surface of the asymmetric metasurface structure, and the dependence of frequency shift of TD_2 on the analyte thickness is investigated and presented in Figure 8A. As the analyte thickness increases from 0 μm (without analyte) to 10 μm, TD_2 experiences a red shift, and the corresponding frequency shift increases almost linearly from 0 to 292 GHz. Frequency shift here is calculated as $f(t) - f(t_0)$, where $f(t)$ is the resonance frequency with analyte thickness t, and $f(t_0)$ is the resonance frequency with the analyte thickness $t_0 = 0\,\mu m$. However, continuing to increase the analyte thickness from 10 to 20 μm, the

frequency shift slowly increases to a saturated value of 15 μm and since then no obvious change can be observed, shown as the green shaded area. The sharp increase of frequency shift for the lower thickness is because the analyte is located in the gaps of the cylinders in which the electric field is intensively confined. In this case, the interaction between the electric field and the analyte gets stronger that causes an increasing red shift as the thickness increases. The saturation of frequency shift for the higher thickness is due to the fact that part of the analyte is situated in an area where fringing electric field mainly distributes. Once the fringing electric field above a certain height from the metasurface surface disappear, there is no interaction between the fringing electric field and the analyte, and thus no red shift can be observed even with the increase of analyte thickness. These results demonstrate that the asymmetric metasurface structure is extremely sensitive to the small change in thickness of thin analyte and thus enhance its application potential for the determination of small volume of analyte. We also analyzed the sensitivity (S) of TD_2 used for the detection of thin analyte by varying the refractive index of analyte, and the sensitivity is compared with that of MD. Figure 8B shows the changes in frequency shift of TD_2 with the increasing refractive index for three cases, the dashed lines are the linear fittings. As the refractive index of analyte with a saturated thickness of 15 μm increases from 1.0 to 2.0, the frequency shift of MD increases to 89 GHz, while the frequency shift of TD_2 can reach 486 GHz. The corresponding sensitivities for MD and TD_2 are 92 GHz/RIU and 489 GHz/RIU, respectively. In this case, the sensitivity of TD_2 has enhanced by 5.3 times compared to that of MD. For the analyte having thin thickness of 4 μm, the frequency shift of TD_2 reaches up to 134 GHz as the refractive index
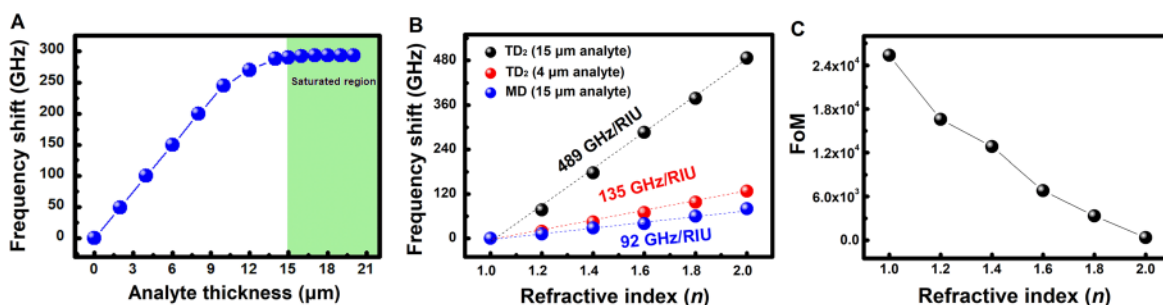

Figure 8: (A) The frequency shift of TD_2 versus the thickness of analyte ($n = 1.6$), the green shaded area is saturated region. (B) The frequency shifts of TD_2 with 15 μm analyte (the black balls) and 4 μm analyte (the red balls), and of MD with 15 μm analyte (the blue balls) deposited on the asymmetric metasurface surface versus the refractive index of analyte, the dashed lines are the linear fittings. (C) The FoMs of TD_2 with 15 μm analyte deposited on the asymmetric metasurface surface versus the refractive index of analyte.

increases from 1.0 to 2.0, which corresponds the sensitive of 135 GHz/RIU. It is noteworthy that this sensitivity is still higher than that of MD in the case of 15 μm analyte deposition. In this case, the equivalent sensitivity of TD_2 for per micrometer thickness of the analyte can be calculated as 34 GHz/RIU. Note that a high sensitivity cannot ensure an excellent sensing performance if the linewidth of resonance is board. Given that, we estimate the FoM to quantitative evaluation the performance of TD_2 for the sensing of 15 μm thick analyte. Figure 8C shows the change of FoM with the refractive index of analyte increasing, the FoM is defined as FoM $= S/FWHM = S \times Q/f(n)$ [55], where S is the sensitivity, and $f(n)$ is the resonance frequency with the analyte refractive index n. The calculated FoM decreases from 25,352 to 360 with refractive indices increasing from 1.0 to 2.0. Ultimately, a comparison of the performance of our proposed metasurface to those of state-of-the art THz metasurface sensors [8, 37, 38, 56–60] is presented in Table 1. Obviously, our structure having high sensitivity and ultrahigh FoM shows its great superiority in sensing application over the previous works. It is worth noting that the sensitivity of THz metasurface based on spoof surface plasmons [60] is higher than that of our structure, however, its FoM is much lower than our structure. The FoM is more meaningful to evaluate the performance of the sensor because it is concerned about not only the sensitivity but also the Q factor. For sensing application, a high-Q factor feature is typically desired to detect a small frequency shift that arises due to the low volume of the analyte or the weak environmental variation. Therefore, with its high sensitivity and ultrahigh FoM, our proposed asymmetric metasurface structure has prominent superiority and huge potential ultrasensitive sensing application at THz frequencies. Therefore, with its high sensitivity and ultrahigh FoM, our proposed asymmetric metasurface structure is suitable for ultrasensitive sensing application at THz frequencies.

4 Conclusion

We propose an ultrasensitive THz sensor based on TD resonance governed by BIC in asymmetric all-dielectric metasurface structure. By elaborately perturbing two cylinders and forming a spatially asymmetric tetramer cluster, two TD resonances that are derived from intracluster TD mode and intercluster TD mode can be excited. The electromagnetic field at resonances is intensively confined in the gaps among the cylinders. These TD resonances exhibit a typical symmetry protected BIC character and have an infinite lifetime. They could transform into TD quasi-BIC resonances with ultrahigh-Q factor of 1.2×10^5 via manipulating the asymmetric parameter. The sensing of analyte shows that the sensitivity of TD resonance in this THz sensor is 489 GHz/RIU for analyte thickness of 15 μm, and is 135 GHz/RIU for analyte thickness of 4 μm, which are higher than previously reported THz all-dielectric metasurface sensor, and the corresponding FoM is up to 25,352. Significantly, our asymmetric metasurface structure with ultrahigh-Q factor is competent to detect a minute frequency shift that arises due to the low volume of the analyte and thus is applicable to detect trace analyte. Moreover, compared to the reported asymmetric metasurface structure realized by making the cylinder height different, our asymmetric metasurface structure is achieved by moving two cylinders, reducing the complexity of the device fabrication. We believe that the proposed metasurface structure can perform superior performance for label-free sensing in the THz region.

Table 1: The list for the performances of THz metasurface sensors including type of metasurface, material of structured layer, analyte, sensitivity, and FoM of the developed systems.

Ref.	Type of metasurface	Material of structured layer	Analyte	Sensitivity (GHz/RIU)	FoM
[38]	TD resonance	Aluminium	Dielectric layer	27.3	
[56]	Fano resonance-BIC	Silicon	Dielectric layer	77	11.1
[57]	Fano resonance	Gold	Dielectric layer	105	7.51
[58]	Perfect absorber	Aluminium	Dielectric layer	139.2	
[59]	EIT resonance	Graphene	Dielectric layer	177.7	59.3
[8]	EIT resonance	Silicon	Dielectric layer	266	64.7
[37]	TD resonance	$LiTaO_3$	Dielectric layer	438	515
[60]	Spoof surface plasmons	Gold	Dielectric layer	1966	19.86
This work	TD resonance-BIC	$LiTaO_3$	Dielectric layer	489	25,352

EIT, electromagnetically induced transparency.

References

[1] M. Tonouchi, "Cutting-edge terahertz technology," *Nat. Photonics*, vol. 1, pp. 97–105, 2007.

[2] J. F. Federici, B. Schulkin, F. Huang, et al., "THz imaging and sensing for security applications—explosives, weapons and drugs," *Semicond. Sci. Technol.*, vol. 20, pp. S266–S280, 2005.

[3] S. Koenig, D. Lopez-Diaz, J. Antes, et al., "Wireless sub-THz communication system with high data rate," *Nat. Photonics*, vol. 7, pp. 977–981, 2013.

[4] L. Ho, M. Pepper, and P. Taday, "Signatures and fingerprints," *Nat. Photonics*, vol. 2, pp. 541–543, 2008.

[5] K. Kawase, Y. Ogawa, Y. Watanabe, and H. Inoue, "Non-destructive terahertz imaging of illicit drugs using spectral fingerprints," *Opt. Express*, vol. 11, pp. 2549–2554, 2003.

[6] M. Brucherseifer, M. Nagel, P. Haring Bolivar, H. Kurz, A. Bosserhoff, and R. Büttner, "Label-free probing of the binding state of DNA by time-domain terahertz sensing," *Appl. Phys. Lett.*, vol. 77, pp. 4049–4051, 2000.

[7] X. Shi and Z. Han, "Enhanced terahertz fingerprint detection with ultrahigh sensitivity using the cavity defect modes," *Sci. Rep.*, vol. 7, p. 13147, 2017.

[8] T. Ma, Q. Huang, H. He, Y. Zhao, X. Lin, and Y. Lu, "All-dielectric metamaterial analogue of electromagnetically induced transparency and its sensing application in terahertz range," *Opt. Express*, vol. 27, pp. 16624–16634, 2019.

[9] V. Astley, K. S. Reichel, J. Jones, R. Mendis, and D. M. Mittleman, "Terahertz multichannel microfluidic sensor based on parallel-plate waveguide resonant cavities," *Appl. Phys. Lett.*, vol. 100, p. 231108, 2012.

[10] W. Wang, F. Yan, S. Tan, H. Zhou, and Y. Hou, "Ultrasensitive terahertz metamaterial sensor based on vertical split ring resonators," *Photonics Res.*, vol. 5, p. 571, 2017.

[11] S. Jahani and Z. Jacob, "All-dielectric metamaterials," *Nat. Nanotechnol.*, vol. 11, pp. 23–36, 2016.

[12] J. A. Schuller, R. Zia, T. Taubner, and M. L. Brongersma, "Dielectric metamaterials based on electric and magnetic resonances of silicon carbide particles," *Phys. Rev. Lett.*, vol. 99, p. 107401, 2007.

[13] Q. Zhao, J. Zhou, F. Zhang, and D. Lippens, "Mie resonance-based dielectric metamaterials," *Mater. Today*, vol. 12, pp. 60–69, 2009.

[14] Q. Yang, X. Chen, Q. Xu, et al., "Broadband terahertz rotator with an all-dielectric metasurface," *Photonics Res.*, vol. 6, p. 1056, 2018.

[15] O. Mitrofanov, T. Siday, R. J. Thompson, T. S. Luk, I. Brener, and J. L. Reno, "Efficient photoconductive terahertz detector with all-dielectric optical metasurface," *APL Photonics*, vol. 3, p. 051703, 2018.

[16] X. Liu, K. Fan, I. V. Shadrivov, and W. J. Padilla, "Experimental realization of a terahertz all-dielectric metasurface absorber," *Opt. Express*, vol. 25, pp. 191–201, 2017.

[17] N. Papasimakis, V. A. Fedotov, V. Savinov, T. A. Raybould, and N. I. Zheludev, "Electromagnetic toroidal excitations in matter and free space," *Nat. Mater.*, vol. 15, pp. 263–71, 2016.

[18] V. Savinov, V. A. Fedotov, and N. I. Zheludev, "Toroidal dipolar excitation and macroscopic electromagnetic properties of metamaterials," *Phys. Rev. B*, vol. 89, p. 205112, 2014.

[19] M. Gupta and R. Singh, "Toroidal versus Fano resonances in high Q planar THz metamaterials," *Adv. Opt. Mater.*, vol. 4, pp. 2119–2125, 2016.

[20] N. Talebi, S. Guo, and P. A. van Aken, "Theory and applications of toroidal moments in electrodynamics: their emergence, characteristics, and technological relevance," *Nanophotonics*, vol. 7, pp. 93–110, 2018.

[21] T. Kaelberer, V. Fedotov, N. Papasimakis, D. Tsai, and N. Zheludev, "Toroidal dipolar response in a metamaterial," *Science*, vol. 330, pp. 1510–1512, 2010.

[22] A. Ahmadivand, B. Gerislioglu, R. Ahuja, and Y. Kumar Mishra, "Terahertz plasmonics: the rise of toroidal metadevices towards immunobiosensings," *Mater. Today*, vol. 32, pp. 108–130, 2020.

[23] A. Ahmadivand, *Toroidal Metamaterials: Fundamentals, Devices, and Applications*, Switzerland AG, Springer Nature, 2020.

[24] A. Ahmadivand, B. Gerislioglu, R. Ahuja, and Y. K. Mishra, "Toroidal metaphotonics and metadevices," *Laser Photonics Rev.*, vol. 14, p. 1900326, 2020.

[25] A. K. Ospanova, G. Labate, L. Matekovits, and A. A. Basharin, "Multipolar passive cloaking by nonradiating anapole excitation," *Sci. Rep.*, vol. 8, p. 12514, 2018.

[26] T. A. Raybould, V. A. Fedotov, N. Papasimakis, et al., "Toroidal circular dichroism," *Phys. Rev. B*, vol. 3, p. 035119, 2016.

[27] K. Marinov, A. D. Boardman, V. A. Fedotov, and N. Zheludev, "Toroidal metamaterial," *New J. Phys.*, vol. 9, pp. 324–324, 2007.

[28] S. Xu, A. Sayanskiy, A. S. Kupriianov, et al., "Experimental observation of toroidal dipole modes in all-dielectric metasurfaces," *Adv. Opt. Mater.*, vol. 7, p. 1801166, 2018.

[29] Y. Fan, Z. Wei, H. Li, H. Chen, and C. M. Soukoulis, "Low-loss and high-Q planar metamaterial with toroidal moment," *Phys. Rev. B*, vol. 87, p. 115417, 2013.

[30] A. A. Basharin, M. Kafesaki, E. N. Economou, et al., "Dielectric metamaterials with toroidal dipolar response," *Phys. Rev. X*, vol. 5, p. 011036, 2015.

[31] M. Gupta, V. Savinov, N. Xu, et al., "Sharp toroidal resonances in planar terahertz metasurfaces," *Adv. Mater.*, vol. 28, pp. 8206–8211, 2016.

[32] V. R. Tuz, V. V. Khardikov, and Y. S. Kivshar, "All-dielectric resonant metasurfaces with a strong toroidal response," *ACS Photonics*, vol. 5, pp. 1871–1876, 2018.

[33] A. Ahmadivand and B. Gerislioglu, "Directional toroidal dipoles driven by oblique poloidal and loop current flows in plasmonic

meta-atoms," *J. Phys. Chem. C*, vol. 122, pp. 24304–24308, 2018.

[34] A. Sayanskiy, M. Danaeifar, P. Kapitanova, and A. E. Miroshnichenko, "All-dielectric metalattice with enhanced toroidal dipole response," *Adv. Opt. Mater.*, vol. 6, p. 1800302, 2018.

[35] Z. G. Dong, J. Zhu, J. Rho, et al., "Optical toroidal dipolar response by an asymmetric double-bar metamaterial," *Appl. Phys. Lett.*, vol. 101, p. 144105, 2012.

[36] J. Li, J. Shao, Y. H. Wang, M. J. Zhu, J. Q. Li, and Z. G. Dong, "Toroidal dipolar response by a dielectric microtube metamaterial in the terahertz regime," *Opt. Express*, vol. 23, pp. 29138–29144, 2015.

[37] X. Chen and W. Fan, "Ultrahigh-Q toroidal dipole resonance in all-dielectric metamaterials for terahertz sensing," *Opt. Lett.*, vol. 44, pp. 5876–5879, 2019.

[38] M. Gupta, Y. K. Srivastava, M. Manjappa, and R. Singh, "Sensing with toroidal metamaterial," *Appl. Phys. Lett.*, vol. 110, p. 121108, 2017.

[39] K. Koshelev, S. Lepeshov, M. Liu, A. Bogdanov, and Y. Kivshar, "Asymmetric metasurfaces with high-Q resonances governed by bound states in the continuum," *Phys. Rev. Lett.*, vol. 121, p. 193903, 2018.

[40] K. Koshelev, G. Favraud, A. Bogdanov, Y. Kivshar, and A. Fratalocchi, "Nonradiating photonics with resonant dielectric nanostructures," *Nanophotonics*, vol. 8, pp. 725–745, 2019.

[41] S. Li, C. Zhou, T. Liu, and S. Xiao, "Symmetry-protected bound states in the continuum supported by all-dielectric metasurfaces," *Phys. Rev.*, vol. 100, p. 063803, 2019.

[42] V. V. Khardikov, E. O. Iarko, and S. L. Prosvirnin, "Trapping of light by metal arrays," *J. Opt.*, vol. 12, p. 045102, 2010.

[43] K. Koshelev, Y. Tang, K. Li, D.-Y. Choi, G. Li, and Y. Kivshar, "Nonlinear metasurfaces governed by bound states in the continuum," *ACS Photonics*, vol. 6, pp. 1639–1644, 2019.

[44] X. Wang, S. Li, and C. Zhou, "Polarization-independent toroidal dipole resonances driven by symmetry-protected BIC in ultraviolet region," *Op. Express*, vol. 28, p. 11983, 2020.

[45] Z. Zhang, Q. Yang, M. Gong, and Z. Long, "Toroidal dipolar bound state in the continuum and antiferromagnetic in asymmetric metasurface," *J. Phys. D: Appl. Phys.*, vol. 53, p. 075106, 2019.

[46] Y. He, G. Guo, T. Feng, Y. Xu, and A. E. Miroshnichenko, "Toroidal dipole bound states in the continuum," *Phys. Rev. B*, vol. 98, p. 161112, 2018.

[47] L. Cong and R. Singh, "Symmetry-protected dual bound states in the continuum in metamaterials," *Adv. Opt. Mater.*, vol. 7, p. 1900383, 2019.

[48] A. Kodigala, T. Lepetit, Q. Gu, B. Bahari, Y. Fainman, and B. Kante, "Lasing action from photonic bound states in continuum," *Nature*, vol. 541, pp. 196–199, 2017.

[49] H. M. Doeleman, F. Monticone, W. den Hollander, A. Alù, and A. F. Koenderink, "Experimental observation of a polarization vortex at an optical bound state in the continuum," *Nat. Photonics*, vol. 12, pp. 397–401, 2018.

[50] Y. K. Srivastava, R. T. Ako, M. Gupta, M. Bhaskaran, S. Sriram, and R. Singh, "Terahertz sensing of 7 nm dielectric film with bound states in the continuum metasurfaces," *Appl. Phys. Lett.*, vol. 115, p. 151105, 2019.

[51] A. Ahmadivand, B. Gerislioglu, Z. Ramezani, and S. A. Ghoreishi, "Attomolar detection of low-molecular weight Antibiotics using midinfrared-resonant toroidal plasmonic metachip technology," *Phys. Rev. Appl.*, vol. 12, p. 034018, 2019.

[52] COMSOL, "RF module," https://www.comsol.com/rf-module.

[53] S. Q. Li and K. B. Crozier, "Origin of the anapole condition as revealed by a simple expansion beyond the toroidal multipole," *Phys. Rev. B*, vol. 97, p. 245423, 2018.

[54] E. E. Radescu and G. Vaman, "Exact calculation of the angular momentum loss, recoil force, and radiation intensity for an arbitrary source in terms of electric, magnetic, and toroid multipoles," *Phys. Rev. E*, vol. 65, p. 046609, 2002.

[55] L. J. Sherry, S. H. Chang, G. C. Schatz, R. P. Van Duyne, B. J. Wiley, and Y. Xia, "Localized surface plasmon resonance spectroscopy of single silver nanocubes," *Nano Lett.*, vol. 5, pp. 2034–2038, 2005.

[56] Y. Zhong, L. Du, Q. Liu, et al., "Ultrasensitive specific sensor based on all-dielectric metasurfaces in the terahertz range," *RSC Adv.*, vol. 10, pp. 33018–33025, 2020.

[57] Q. Xie, G. X. Dong, B. X. Wang, and W. Q. Huang, "High-Q Fano resonance in terahertz frequency based on an asymmetric metamaterial resonator," *Nanoscale Res. Lett.*, vol. 13, p. 294, 2018.

[58] R. Yahiaoui, S. Tan, L. Cong, R. Singh, F. Yan, and W. Zhang, "Multispectral terahertz sensing with highly flexible ultrathin metamaterial absorber," *J. Appl. Phys.*, vol. 118, p. 083103, 2015.

[59] X. He, Q. Zhang, G. Lu, G. Ying, F. Wu, and J. Jiang, "Tunable ultrasensitive terahertz sensor based on complementary graphene metamaterials," *RSC Adv.*, vol. 6, pp. 52212–52218, 2016.

[60] X. Chen and W. Fan, "Ultrasensitive terahertz metamaterial sensor based on spoof surface plasmon," *Sci. Rep.*, vol. 7, p. 2092, 2017.